Novel method for in situ damage monitoring during ultrasonic fatigue testing by the advanced acoustic emission technique

M. Seleznev[a]*, A. Weidner[a], H. Biermann[a], A. Vinogradov[b]

[a]*Institute of Materials Engineering, TU Bergakademie Freiberg, Gustav-Zeuner-Straße 5, D-09599 Freiberg, Germany*

[b]*Department of Mechanical and Industrial Engineering, Norwegian University of Science and Technology, NO-7491 Trondheim, Norway*

* Corresponding author, E-mail address: mikhail.seleznev@iwt.tu-freiberg.de (M. Seleznev).

ABSTRACT

Ultrasonic fatigue testing (USFT) is an effective method for the rapid characterisation of the high cycle fatigue properties of structural materials. However, the process of initiation and progression of fatigue damage remains uncertain in this way of testing due to the limitations of existing measuring techniques. The acoustic emission (AE) method was applied and developed in the present work to pave a new way to monitor the fatigue process during USFT. The proposed new methodology revealed the AE activity related to fatigue damage, allowing to distinguish between surface and internal fatigue crack initiation and to follow the development of fatigue damage.

Keywords: high frequency testing; high cycle fatigue; acoustic emission; aluminium alloys; fatigue test methods.

Introduction

Along with the increasing severity of operation conditions, the service life of engineering components moves towards high and very high cycle fatigue (HCF, VHCF), thus stimulating more and more stringent requirements for reliable fatigue properties. To meet these demands, a deeper understanding is needed of the microstructural mechanisms of cyclic deformation, crack initiation and growth in the high/very-high cyclic regime [1]. The progress in this field depends heavily on the capacity of modern techniques aiming at identifying the initial fatigue damage, which is particularly challenging at small applied cyclic strains/stresses. The effective way of assessing the fatigue resistance of metals beyond HCF is the ultrasonic fatigue testing (USFT) method [2,3], which enjoys the burgeoning research activity nowadays. However, due to preferentially internal fatigue crack initiation and growth at small stress amplitudes in HCF and VHCF regime, the direct observation of early stages of the crack development is impossible.

Among many indirect non-destructive (NDT) methods devised for the fatigue damage evaluation (potential drop [4], ultrasonic [5,6] including hysteresis damping [7], infrared thermography [8], etc.), acoustic emission (AE) is one of the most versatile and sensitive [9]. It has been widely used for in-situ characterisation of various materials (metals [10], concrete [11], composites [12], etc.) and structures (aerospace gears [13], wind turbine blades [14], etc.) under cyclic stresses. Whereas the use of the AE technique during conventional low-frequency cyclic loading is a classic topic in the field of the AE research [15–17],

the AE method has not been applied to USFT so far, to the best of our knowledge. The likely reason for this is the severe noise level of the ultrasonic experimental setup interfering strongly with the AE frequency response. This noise cannot be rejected by the cut-off or band-pass filters that equip most of the commercially available AE systems. The persistent advances in computational power and data mining tools enabled complex signal processing to be implemented to recover useful information from the noisy AE waveforms. Considering the urgent need for the NDT method of damage monitoring and assessment during USFT, this encouraged us to develop a new AE-powered platform for the analysis of the fatigue damage progress during ultrasonic testing.

Experimental Methodology

The commercial alloy AlSi9Cu3 (EN AC 46000) was used for fatigue testing (Fig. 1). The alloy was remelted and cast into cylinders which then undergone hot isostatic pressing (HIP) to close casting cavities. The chemical composition measured by optical emission spectroscopy (Table 1) determines the alloy's microstructure, which consists of three main phases – the Al matrix, Al-Si eutectic and α-Al(Fe, Mn)Si intermetallic compound with either polyhedral or "Chinese script" morphology (Fig. 1b) [18]. The large brittle α-phase polyhedrons served as stress risers and crack initiators, whereas the ductile matrix enables crack blunting, and controls the crack growth rate. Specimens for USFT were designed to have a resonant frequency F_{res} = 19.5 kHz and turned from the cylinders after HIP (Fig. 1a). The central gauge parts were polished to a mirror finish to facilitate the sub-surface crack initiation.

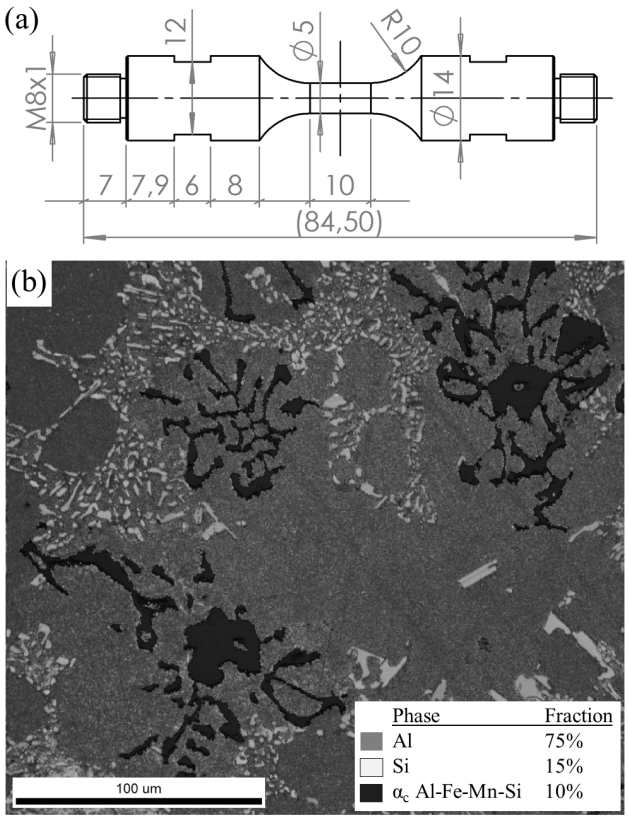

The resonant axial fatigue tests were performed using the USFT-device (BOKU, Austria) under the loading conditions with positive mean stresses (loading ratio $R = 0.1$) in air (Fig. 2). The threaded specimens were mounted to the resonating module and preloaded statically using the screw-driven frame (Hegewald&Peschke, Germany). The continuous mode cyclic loading was provided by the piezo actuator generating the standing longitudinal waves, which were amplified by the Titanium horn and vibration-controlled by the feedback signal from the vibration sensor. In-situ thermal imaging and compressed air cooling were used to maintain the specimen temperature at 20±2 °C.

Table 1. The chemical composition (values in weight %) of investigated AlSi9Cu3 alloy

Si	Fe	Cu	Mn	Mg	Ni	Zn	Ti	Pb	Al
8.73	0.99	2.15	0.47	0.21	0.05	0.42	0.04	0.5	rest

The PCI-2-based AE system by Physical Acoustics Corp. (USA) was used to acquire the AE waveforms. The broadband AE sensor PICO was attached to the loose end of the tensile rod connected to the loaded specimen. The AE signal was amplified by 40 dB with the low-noise 2/4/6 preamplifier, passed through the 50-1000 kHz band-pass filter and recorded in a continuous threshold-less mode by the 18-bit PCI-2 board with the sampling frequency of 2 MHz. All signal processing algorithms were implemented in MATLAB.

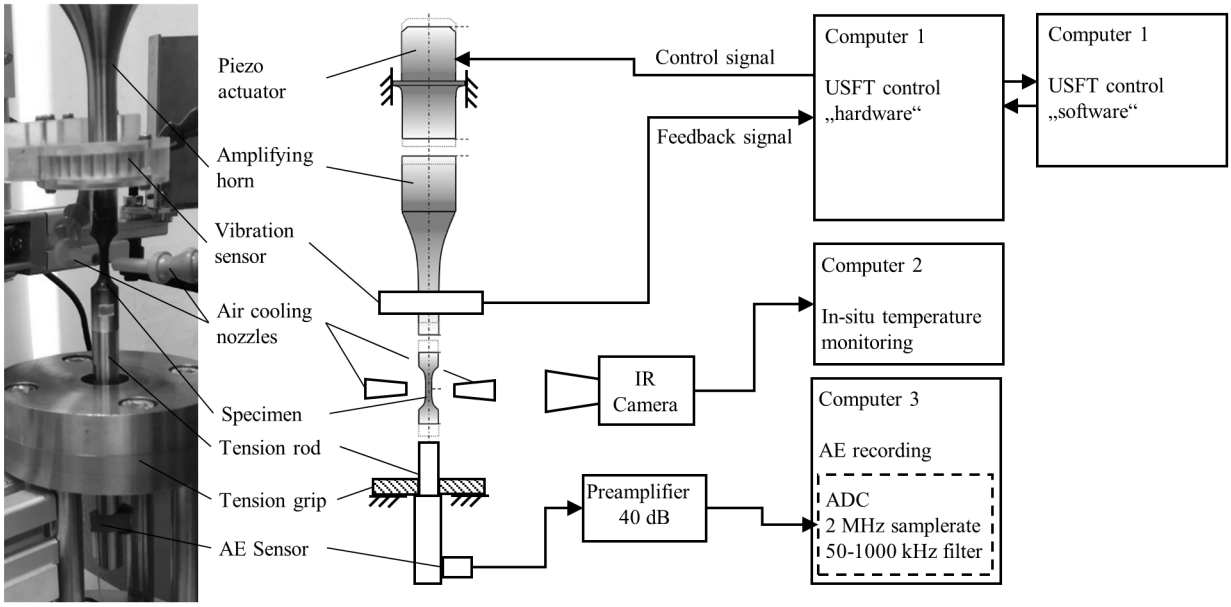

Fig. 2. /*double column, grayscale*/ Graphical summary of the experimental setup which includes a photographic image of the resonating block (on the left), its simplified principal scheme and parts description (in the middle), and control units (on the right).

Ten cyclic loading tests were performed at the stress amplitude $\sigma_a = 70\pm2$ MPa resulting randomly in fatigue failure due to either the surface or internal crack, initiated from α-phase polyhedrons. The number of cycles to failure N_f ranged within 5×10^6 – 3×10^7. Fatigue failure was detected automatically by the USFT control system when the vibration amplitude remained below 85 % of the pre-set level for more than 100 ms. Several tests, where AE was not detected after a few million cycles, were

terminated to verify the absence of fatigue damage. All fatigued specimens were cooled in liquid nitrogen and artificially fractured to reveal the signatures of fatigue on the fracture surface. The fractographic analysis was performed by means of scanning electron microscopy (SEM) with backscattered electron (BSE) imaging used to highlight the crack initiating particles. Low-magnification optical microscopy (OM) was used to identify the fatigue fracture zones distinguishable according to their specific colours caused by the differences in the oxidation rate.

For easy handling of large datasets, the continuous AE waveform was recorded as a series of consecutive streams of 1 min duration each. The signal processing applied to each stream is described in brief by the flow-chart shown in Fig. 3. The short-time Fourier transformation (STFT) was used to decompose the raw signal in the time-frequency domain and to obtain the spectrogram (magnitude squared of the STFT) representation of the power spectral density (PSD) of the signal. A whole stream was divided into consecutive segments of 2048 readings using the Blackman window with 80 % overlap and the discrete Fourier transform (DFT) applied to each segment. The obtained "raw" spectrogram demonstrates the periodic horizontal lines corresponding to the maxima of the PSD function. These peaks are related to the resonance modes at frequencies $n \cdot F_{res}$, where n is an integer number.

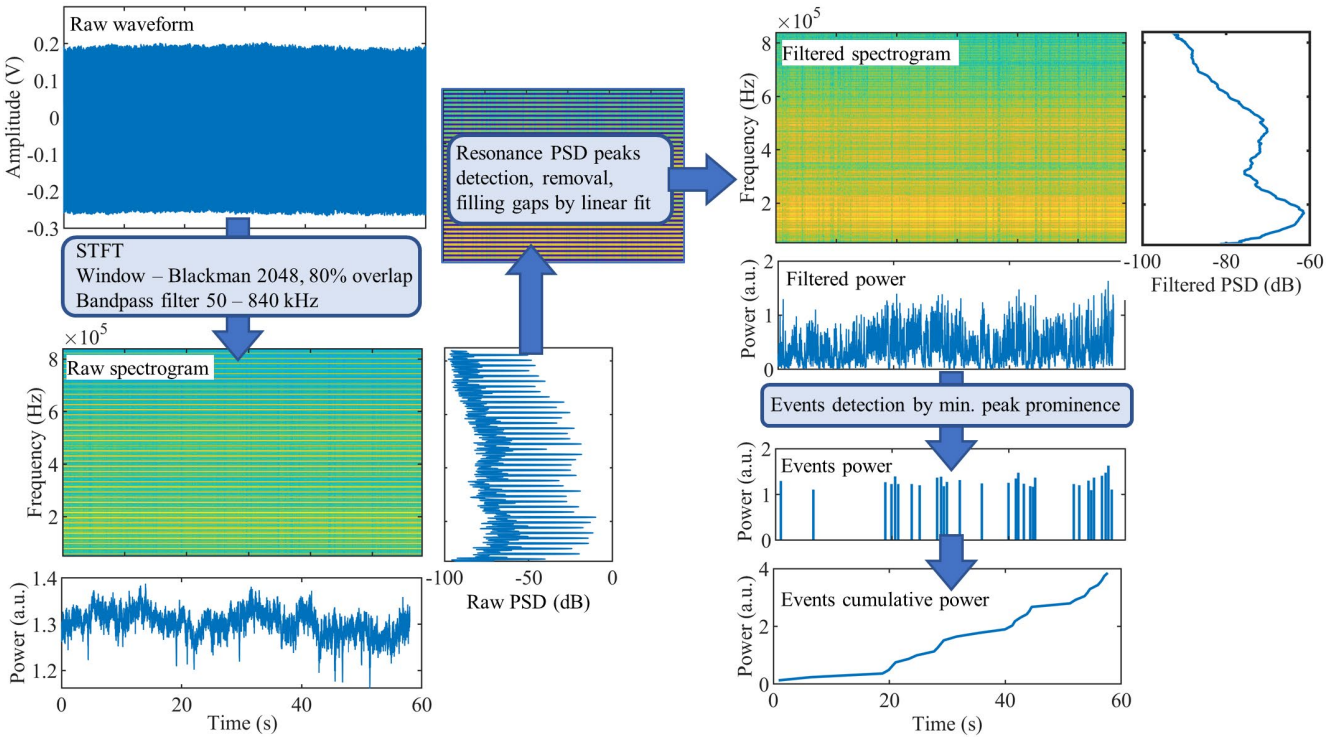

Fig. 3. */double column, colour online/* Flow chart of the processing algorithm designed for analysis of the continuous acoustic emission signal acquired during ultrasonic fatigue testing, according to Fig. 2.

To increase the signal-to-noise ratio of the cumulative AE power envelope (which is a sum of the power frequency components along each vertical (time) line of the spectrogram), resonance peaks must be filtered out. This can be done by using a general peak detection algorithm (e.g. searching for the maximum in the defined interval, or see [19] for advanced peak

detectors), removing peak-related values from the spectrogram and filling gaps by the linear regression. The spectrograms and PSDs adaptively filtered in this way are free from the sharp resonance peaks, and, therefore, the power envelope can be used for AE events detection. The detection method implemented in the present work is based on the minimum peak prominence, which is defined as a triple value of the median signal power within the first recorded AE stream.

Results and Discussion

All experimental findings fall logically into three categories depending on the fatigue failure mode governed either by (i) the surface crack initiation (SCI), or (ii) internal crack initiation (ICI). Alternatively, (iii) no detectable fatigue damage was observed in several tests. These three scenarios are exemplified in Fig. 4 on the left, middle, and right columns, respectively. The presented examples are typical. For more illustrations of the characteristic AE behaviour accompanying the surface and sub-surface crack initiation and propagation, the readers are encouraged to review Supplementary Materials. The graphs in the first row (Fig. 4a - c) demonstrate the behaviour of the resonance-based parameters, which are commonly used in the USFT analysis - the resonance frequency F_{res} and relative nonlinearity parameter $\beta_{rel} = (A_2 - 2A_1) - (A_2(0) - 2A_1(0))$, where A_1 and A_2 are the amplitudes in dB at the second-harmonic and fundamental frequencies, respectively [5], $A_1(0)$ and $A_2(0)$ are their values at the beginning of the cyclic load. Shortly before the fatigue failure occurs, F_{res} drops since the developing major crack reduces the gauge cross-section. In contrary, the β_{rel} value rises up from nearly zero up to 100 – 150 dB in response to the progressing failure. These two parameters can, in principle, indicate the progressive failure, albeit with different confidence (c.f. the behaviour of β_{rel} in Figs. 4a and b). Nonetheless, either of them fails to detect the very early stages of damage initiation due to the high susceptibility to fluctuations in air-cooling, ambient temperature, etc.

The variations in the AE amplitude envelope (Fig. 4d – f) might be related to damage, although in a quite inconclusive way. The application of the proposed signal processing scheme (Fig. 3) unveils the apparent correlation between the power of the detected AE events, as well as their accumulation rate, with the progressive material damage. Indeed, when cyclic loading resulted in fatigue failure (Fig. 4j, k), the pronounced AE activity is observed (Fig. 4g, h). As opposes to this, when no signatures of damage are noticed in the behaviour of the mechanical resonance parameters (Fig. 4c), and, concomitantly, no fatigue damage is seen in the fracture surface after artificial fracture (Fig. 4l), the AE ceases to occur (Fig. 4i). In most cases, the event detection algorithm reveals the AE activity notably earlier than any appreciable changes occur in the raw AE waveform, F_{res} or β_{rel} (Fig. 4j). Figure 4b, e, h illustrates the exceptional case where the onset of the AE activity agrees well with the slope rise in β_{rel}. This coincidence can be, however, fully accidental and misleading if β_{rel} is taken as the primary damage indicator since the similar slope rise of β_{rel} visible in Fig. 4c is obviously not related to any fatigue damage or AE activity. Although the resonant-based parameters can serve as established criteria of the late-stage fatigue, they can hardly deliver any conclusive information on the damage accumulation process. As opposed to this, AE reflects primary stages of fatigue progression with confidence based on

the comparison of the characteristic AE behaviour and fracture surface features for different failure situations represented in Fig. 4.

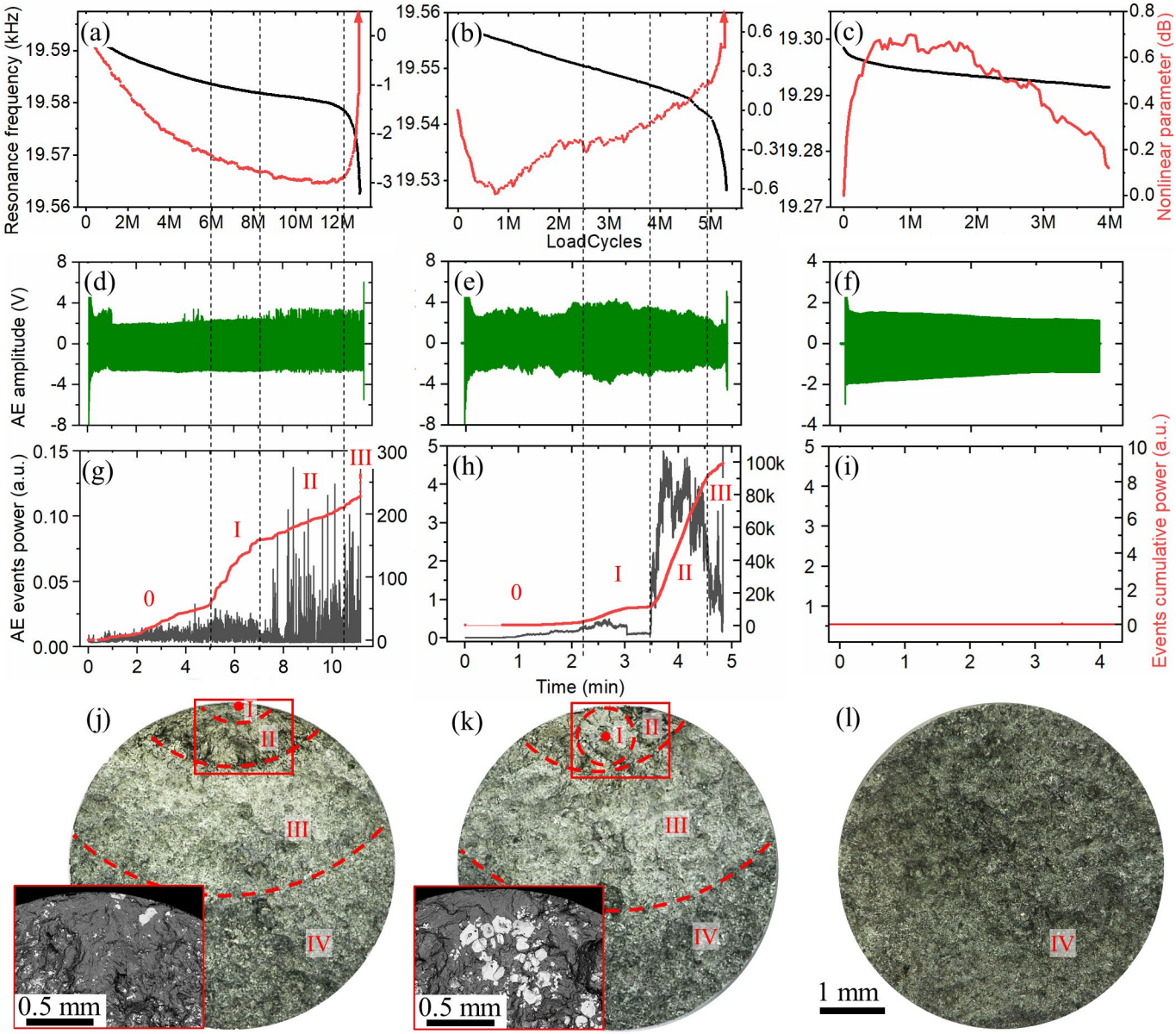

Fig. 4. /*double column, colour online*/ Illustration of the application of the proposed AE-based damage monitoring technique to the ultrasonic fatigue testing of the AlSi9Cu3 alloy. The raw AE waveforms (d - f) are processed according to the scheme shown in Fig. 3 and the results of the signal power extraction (g – i, grey curves) are compared to the resonance-based parameters (a - c), and are aligned with fracture morphologies obtained by means of optical microscopy (j - l) and backscattered electron imaging (BSE) of the crack initiation sites (insets in j, k). The left column (a, d, g, j) represents the case of typical surface crack initiation, the middle column (b, e, h, k) exemplifies the case of internal (sub-surface) crack initiation, and the right column (c, f, i, l) shows the example where the experiment was interrupted without detected fatigue damage. Fracture morphology areas (j - l) corresponding to stages of fatigue crack evolution (0 - III) and the forced rupture (IV) are correlated with the behaviour of the cumulative power (g – i, red lines).

The cumulative AE power evolution is represented by several almost linear segments with different slopes corresponding to different histories of fatigue damage accumulation. Although the nearly linear trends in the AE behaviour support the hypothesis of the linear damage summation on each stage, the overall fatigue damage process appears to be substantially nonlinear, and four different stages of crack initiation and propagation (0 – III in Figs. 4j, k, l) are discerned due to different rates of the observed damage process as follows.

0) The c*rack initiation* stage (marked by the red dot in Figs. 4j, k) is most likely the result of microstructural damage accumulation due to the stress concentration at the interface between the matrix and α-phase polyhedrons [20]. When the critical damage is reached, the intermetallic particle (or a cluster of particles) breaks in a brittle manner. In both SCI and ICI scenarios, this stage corresponds to the lowest slope of the cumulative power at roughly half of the total fatigue life. This stage can demonstrate a relatively high AE activity (c.f. Fig. 4g, stage 0), which can be explained by the initiation and arresting of multiple microcracks before the critical damage is attained and the final crack initiation site is developed.

I) The s*mooth area* (SA) surrounds fractured α-phase particles. It extends up to 0.5 mm from the epicentre and exhibits similar morphology for both SCI and ICI (fisheye) (c.f. insets in Figs. 4j, k). The stress intensity factor (SIF) range ΔK and the related size of a plane-stress cyclic plastic zone r_c can be estimated according to Murakami [21] and Suresh [22], respectively, for the transition from SA to the next fatigue fracture zone:

$$\Delta K_{SA} \approx 0.65 \cdot \Delta\sigma\sqrt{\pi\sqrt{area_{SA}}} \approx 3.5\ MPa\ \sqrt{m}\,, \quad r_{c\,SA} \approx \frac{1}{2\pi}\left(\frac{\Delta K_{SA}}{2\sigma_{YS}}\right)^2 \approx 42\ \mu m\,, \tag{1}$$

where the stress range $\Delta\sigma = 2\sigma_a = 140$ MPa, total area of SA $area_{SA} \approx 0.2$ mm^2, and the yield stress $\sigma_{YS} = 150$ MPa [23]. SA can be attributed to a mechanically short crack, which propagates approximately along the plane of the maximum normal stresses, thus forming a fisheye-like flat surface until r_c reaches the size of a dendrite arm spacing $D = 34\pm4$ μm, which has been evaluated for the present alloy in [23]. A noteworthy agreement between the experimentally measured dendrite arm spacing and the cyclic plastic zone size at the end of the crack propagation within the SA region is observed.

II) The highly oxidised *dark rough area* forms when $r_c > D$, so that the mechanically short crack can develop beyond one dendrite arm, branching and forming the characteristic relief (Figs. 4j, k, II). The similar fracture mechanics within and beyond SA is also known for steels [24,25]. According to AE results, stage II extends to approximately 3 Mcycles for the SCI (Fig. 4g, II), and only 1 Mcycles for ICI (Fig. 4h, II). This is plausible because, in the case of ICI, the internal crack confined to the fisheye and the cluster of α-phase particles covers the significant part of the stable fatigue crack growth area (stage II). This explains both the smaller number of cycles and the higher AE activity during stage II of the ICI scenario due to the promoted fracture of material between the specimen's surface and the fisheye.

III) The low-oxidised *bright rough area* is clearly separated from stage II and is characteristic of the faster crack propagation rates. Stage III takes place at the threshold SIF range $\Delta K_{th} \geq 5.8$ MPa$\sqrt{\text{m}}$ calculated for both ICI and SCI areas at the end of stage

II using Eq. (1). Here ΔK_{th} denotes the short-to-long fatigue crack transition, whereas the known values of ΔK_{th} for aluminium alloys are within the broad range of 2-5 MPa√m [26–29]. This uncertainty could be due to the application of different approaches in SIF estimation and the rationale standing behind it, as mentioned by Zerbst et al. [30]. The relatively high calculated value of ΔK_{th} could be due to the crack closure effect disregarded in the present analysis. According to the AE results, stage III takes approximately 0.5-1 Mcycles for the given examples. The onset of this stage (Figs. 4g, h, III) matches correctly with the critical change in the resonance parameters (Figs. 4a, b).

IV) The artificially-induced cryogenic *rupture* gives rise to a clearly visible rough fracture surface with almost no oxidation (Figs. 4j, k, l, IV).

The difference between the surface and internal crack initiation scenarios can be seen on the corresponding events cumulative power curves: the highest slope related to the highest AE activity is attributed either to stage I (Fig. 4g), or stage II (Fig. 4h) and can be likely related to the onset of surface fracture (see also examples in Supplementary Materials). A crack originated at the surface emits steady AE signals with magnitudes large enough to be easily detectable after the spectral filtering procedure proposed. In contrary, the AE signals bearing their origin from the internally developing crack are featured by notably lesser amplitudes, at least until the crack reaches the surface. The actual reason for that is unknown. We can suppose that this is due to a constraint effect, the role of which in AE, is, however, unknown and requires a dedicated study. When the internal crack reaches the surface, the remaining ligaments between the fisheye and the surface will rupture intensively, promoting a steep rise in the slope of the cumulative AE power curve.

Conclusions

The application of AE monitoring to USFT is beneficial for the early detection and monitoring fatigue damage. Resonance-related noise in the AE signal recorded from USFT can be successfully eliminated by signal processing involving the STFT time-frequency decomposition of the waveforms followed by the peak detection procedure. The detected AE events strongly correlate with fatigue damage progression. The cumulative power of the detected AE events unveils the stage-like behaviour, which occurs differently for the surface and internal fatigue cracks initiation scenarios. The cumulative AE power can thus serve as an in situ measurable non-destructive damage parameter highlighting the fundamental nonlinearity of fatigue damage accumulation. The proposed method of AE monitoring of ultrasonically loaded metallic component enables unambiguous detection of fatigue damage earlier than the resonance-based methods used conventionally in the ultrasonic fatigue testing.

The proposed signal-processing methodology is applicable not only to aluminium-based alloys and the continuous resonant cycling mode, but it also applies to other metallic materials and the pulse-pause testing mode (results will be published elsewhere). Without limitations, the proposed method can be extended to gigacycle fatigue regimes. Thus, the modern AE

technique can be converted into a versatile tool for investigating both surface and subsurface small fatigue cracks. As a scope of the future work, we intend to establish the direct link between the fatigue degradation stages and AE via step-wise USFT with in-situ AE recording and X-ray computer tomography.

Financial support from the German Research Foundation [Project-ID 169148856 – SFB 920, subproject C04] is gratefully appreciated. The authors would also thank the colleagues from TU Bergakademie Freiberg, in particular the foundry institute for providing the as-cast material and the workshop for manufacturing the fatigue specimens.

References

[1] Mughrabi H. Fatigue, an everlasting materials problem - Still en vogue. Procedia Eng 2010;2:3–26. https://doi.org/10.1016/j.proeng.2010.03.003.

[2] Stanzl-Tschegg SE. Time Saving Method for Measuring VHC Fatigue and Fatigue Crack Growth Data with the Ultrasonic Fatigue Technique. Procedia Struct Integr 2016;2:3–10. https://doi.org/10.1016/j.prostr.2016.06.002.

[3] Zimmermann M. Very High Cycle Fatigue. Handb. Mech. Mater., Singapore: Springer; 2018, p. 1–38.

[4] Si Y, Rouse JP, Hyde CJ. Potential difference methods for measuring crack growth: A review. Int J Fatigue 2020;136. https://doi.org/10.1016/j.ijfatigue.2020.105624.

[5] Kumar A, Torbet CJ, Jones JW, Pollock TM. Nonlinear ultrasonics for in situ damage detection during high frequency fatigue. J Appl Phys 2009;106. https://doi.org/10.1063/1.3169520.

[6] Jhang K. Nonlinear Ultrasonic Techniques for Non- destructive Assessment of Micro Damage in Material : A Review. Int J Precis Eng Manuf 2009;10:123–35.

[7] Lage Y, Cachão H, Reis L, Fonte M, De Freitas M, Ribeiro A. A damage parameter for HCF and VHCF based on hysteretic damping. Int J Fatigue 2014;62:2–9. https://doi.org/10.1016/j.ijfatigue.2013.10.010.

[8] Krewerth D, Lippmann T, Weidner A, Biermann H. Application of full-surface view in situ thermography measurements during ultrasonic fatigue of cast steel G42CrMo4. Int J Fatigue 2015;80:459–67. https://doi.org/10.1016/j.ijfatigue.2015.07.013.

[9] Wadley HNG, Mehrabian R. Acoustic Emission for Materials Processing : a Review. Mater Sci Eng 1984;65:245–63.

[10] Chai M, Zhang J, Zhang Z, Duan Q, Cheng G. Acoustic emission studies for characterization of fatigue crack growth in 316LN stainless steel and welds. Appl Acoust 2017;126:101–13. https://doi.org/10.1016/j.apacoust.2017.05.014.

[11] Noorsuhada MN. An overview on fatigue damage assessment of reinforced concrete structures with the aid of acoustic emission technique. Constr Build Mater 2016;112:424–39. https://doi.org/10.1016/j.conbuildmat.2016.02.206.

[12] Saeedifar M, Zarouchas D. Damage characterization of laminated composites using acoustic emission: A review. Compos Part B Eng 2020;195:108039. https://doi.org/10.1016/j.compositesb.2020.108039.

[13] Holford KM, Eaton MJ, Hensman JJ, Pullin R, Evans SL, Dervilis N, et al. A new methodology for automating acoustic emission detection of metallic fatigue fractures in highly demanding aerospace environments: An overview. Prog Aerosp Sci 2017;90:1–11. https://doi.org/10.1016/j.paerosci.2016.11.003.

[14] Du Y, Zhou S, Jing X, Peng Y, Wu H, Kwok N. Damage detection techniques for wind turbine blades: A review. Mech Syst Signal Process 2020;141:106445. https://doi.org/10.1016/j.ymssp.2019.106445.

[15] Vinogradov A, Hashimoto S, Patlan V, Kitagawa K. Acoustic emission during cyclic deformation of ultrafme- grain copper processed by severe plastic deformation. Philos Mag A Phys Condens Matter, Struct Defects Mech Prop 2002;82:317–35. https://doi.org/10.1080/01418610208239601.

[16] Chai M, Zhang Z, Duan Q. A new qualitative acoustic emission parameter based on Shannon's entropy for damage monitoring. Mech Syst Signal Process 2018;100:617–29. https://doi.org/10.1016/j.ymssp.2017.08.007.

[17] Kotzem D, Arold T, Niendorf T, Walther F. Damage tolerance evaluation of E-PBF-manufactured inconel 718 strut geometries by advanced characterization techniques. Materials (Basel) 2020;13:247. https://doi.org/10.3390/ma13010247.

[18] Becker H, Bergh T, Vullum PE, Leineweber A, Li Y. Effect of Mn and cooling rates on α-, β- and δ-Al–Fe–Si intermetallic phase formation in a secondary Al–Si alloy. Materialia 2019;5. https://doi.org/10.1016/j.mtla.2018.100198.

[19] Scholkmann F, Boss J, Wolf M. An efficient algorithm for automatic peak detection in noisy periodic and quasi-periodic signals. Algorithms 2012;5:588–603. https://doi.org/10.3390/a5040588.

[20] Zerbst U, Madia M, Klinger C, Bettge D, Murakami Y. Defects as a root cause of fatigue failure of metallic components. II: Non-metallic inclusions. Eng Fail Anal 2019;98:228–39. https://doi.org/10.1016/j.engfailanal.2019.01.054.

[21] Murakami Y. Metal Fatigue Effects of Small Defects and Nonmetallic Inclusions. Elsevier Ltd.; 2002.

[22] Suresh S. Fatigue of materials. 2nd ed. Cambridge: University Press; 1998.

[23] Fischer H. Untersuchungen zum einfluss einer schmelzekonditionierung von AlSi9Cu3 auf die mikrostrukturelle ausprägung und die ermüdungslebensdauer. TU Bergakademie Freiberg, 2020.

[24] Seleznev M, Weidner A, Biermann H. On the formation of ridges and burnished debris along internal fatigue crack propagation in 42CrMo4 steel. Fatigue Fract Eng Mater Struct 2020:1–16. https://doi.org/10.1111/ffe.13252.

[25] Seleznev M, Merson E, Weidner A, Biermann H. Evaluation of very high cycle fatigue zones in 42CrMo4 steel with plate-like alumina inclusions. Int J Fatigue 2019;126:258–69. https://doi.org/10.1016/j.prostr.2018.12.206.

[26] Mayer H, Papakyriacou M, Pippan R, Stanzl-Tschegg S. Influence of loading frequency on the high cycle fatigue properties of AlZnMgCu1.5 aluminium alloy. Mater Sci Eng A 2001;314:48–54.

[27] Toda H, Sinclair I, Buffière JY, Maire E, Khor KH, Gregson P, et al. A 3D measurement procedure for internal local crack driving forces via synchrotron X-ray microtomography. Acta Mater 2004;52:1305–17. https://doi.org/10.1016/j.actamat.2003.11.014.

[28] Davidson D, Chan K, McClung R, Hudak S. Small fatigue cracks. Compr. Struct. Integr., 2012, p. 541–69. https://doi.org/10.1017/cbo9780511806575.017.

[29] Xu L, Wang Q, Zhou M. Micro-crack initiation and propagation in a high strength aluminum alloy during very high cycle fatigue. Mater Sci Eng A 2018;715:404–13. https://doi.org/10.1016/j.msea.2018.01.008.

[30] Zerbst U, Madia M, Klinger C, Bettge D, Murakami Y. Defects as a root cause of fatigue failure of metallic components. I: Basic aspects. Eng Fail Anal 2019;97:777–92. https://doi.org/10.1016/j.engfailanal.2019.01.055.